Supporting Information for

# Broadband metallic fiber-to-chip couplers and a low-complexity integrated plasmonic platform

*Andreas Messner,[*,†] Pascal A. Jud,[†] Joel Winiger,[†] Marco Eppenberger,[†] Daniel Chelladurai,[†] Wolfgang Heni,[‡] Benedikt Baeuerle,[‡] Ueli Koch,[†] Ping Ma,[†] Christian Haffner,[†] Huajun Xu,[§] Delwin L. Elder,[§] Larry R. Dalton,[§] Jasmin Smajic,[†] Juerg Leuthold[*,‡,†]*

[†]ETH Zurich, Institute of Electromagnetic Fields (IEF), 8092 Zürich, Switzerland

[‡]Polariton Technologies AG, 8803 Rüschlikon, Switzerland

[§]University of Washington, Department of Chemistry, Seattle, Washington 98195-1700, United States

*Corresponding Authors: amessner@ethz.ch, leuthold@ethz.ch

## 1. Device Layout

A pitch reduced optical fiber array (Chiral Photonics) with 12 µm core-to-core pitch and 2 µm mode field diameter was used to couple light into and from the devices. The discrete core spacing resulted in waveguiding sections of 11, 23 or 35 µm length. The width of the waveguide section is 4 µm, the width of the grating bars is 8 µm, and they are anchored with a larger metallic patch at their ends. The device presented in the main part of the manuscript has a grating period of 800 nm, with a fill factor of 30%.

In case of the active devices, the bottom electrode has been structured such to accommodate an electrical ground-signal-ground probe, see Figure S4(a). Furthermore, the top gold electrode has been electrically connected with a narrow contact, Figure S4(b). Due to the large width of the MIM waveguide, this contact hardly influences the plasmonic mode and the insertion loss of the device. 2D simulations indicate an excess loss of 0.05 dB due to a contact of 1 µm width connected to a 3-µm-wide plasmonic waveguide. In experiment, the influence of the contact could not be determined, as it was smaller than the setup and device-to-device uncertainties.

## 2. Device Fabrication

The passive device has been fabricated as follows. 120 nm of gold has been e-beam evaporated on 6.2 µm thermal $SiO_2$ on a Si substrate. After that, 100 nm of silicon oxynitride ($SiO_xN_y$) has been deposited by a physically enhanced chemical vapor deposition (PECVD) process. As a last step, the metal gratings and waveguide sections have been deposited in a lift-off process, where 200 nm of gold were e-beam evaporated on top of a 1-nm-thick titanium adhesion layer. Finally, the sample was cladded with 500 nm of PMMA.

### Fabrication of the active device

120 nm of gold has been e-beam evaporated on 6.2 µm thermal $SiO_2$ on Si, and structured with a lift-off process to separate the individual device on one chip electrically. After the lift-off, a 10-nm-thick $TiO_2$ layer has been deposited as a charge-blocking layer.[1] A ~140-nm-thick layer of HLD1/HLD2[2] was spin-coated, and 200 nm of gold were e-beam evaporated on top of a 1-nm-thick titanium adhesion layer. A negative resist was exposed in an e-beam lithography step and used to define the gratings and waveguides in a physical dry-etching step. Although the structuring of a gold film on top of an organic electro-optic material posed challenges to us and resulted in a lower coupling efficiency as for the passive devices, these issues are not of fundamental nature and should be solved by improved fabrication processes, or the integration of ferroelectric (solid-state) materials. After the fabrication, the sample was cladded with 500 nm PMMA. Before the electro-optical measurements, the device was electric-field poled by heating it to the glass transition temperature of the employed electro-optic organic material (HLD1/2) while applying the electric poling field.[2, 3]

## 3. Simulations

Two-dimensional Finite Difference Time Domain (FDTD) simulations were used for all simulations carried out in this work.[4] Perfectly matched layer boundary conditions were used at the domain boundaries. The model was excited by launching a fiber mode through a waveguide port, and a second waveguide port was used to determine the transmission into the plasmonic slot ($S_{21}$). The fiber-to-slot coupling efficiency (*CE*) has been determined by subtracting the plasmonic waveguide losses from the port-to-port transmission $S_{21}$. The time-domain excitation was chosen such that a spectral window from 1250 to 1650 nm was covered. Spectrally resolved, complex refractive index data of the employed materials was retrieved from in-house ellipsometry measurements ($SiO_xN_y$, HLD1/2, Au) or literature ($SiO_2$,[5] PMMA[6]).

### Simulation parameters

The measured coupling efficiency spectrum shown in Figure 1 of the main manuscript has been recorded with a device with a grating period of 800 nm, and a fill factor of 30%, that is the fraction of the grating period filled with metal. The simulation in the same plot has been achieved with the same parameters, but the period has been reduced by ~5% to 750 nm to achieve a good fit. We attribute this change of period to fabrication imperfections (such as precise film thicknesses, particularly of the PMMA cladding), and inaccuracies in the used refractive index data.

## 4. Explanation of Transmission Spectrum: Bragg Resonance

The measured spectrum of the coupling efficiency shows a transmission dip at $\lambda \approx 1430$ nm, see Figure 1 of the main text. In the following, we relate the transmission dip to a Bragg resonance of the grating.

Figure S1(a,b) shows the simulated out-of-plane *H*-field component at the transmission maximum (1530 nm) and minimum (1430 nm), respectively. At the left side of the structure, an additional MIM waveguide (labelled MIM Control) has been introduced, to monitor energy that is not directed into the actual MIM waveguide at the right of the structure. We excite the fiber port, and indeed, energy is directed bidirectionally to the left and right at the transmission minimum. This indicates that the grating might have a Bragg passband at this wavelength. To test this hypothesis, we launched a mode from the right MIM port and recorded both the transmission to the fiber port and through the grating towards the second MIM control port. Figure S1(c) shows both transmission spectra. The transmission through the grating (MIM Port to MIM Control), has a maximum exactly where the coupling efficiency has a minimum, and hence shows the behavior of a Bragg passband.

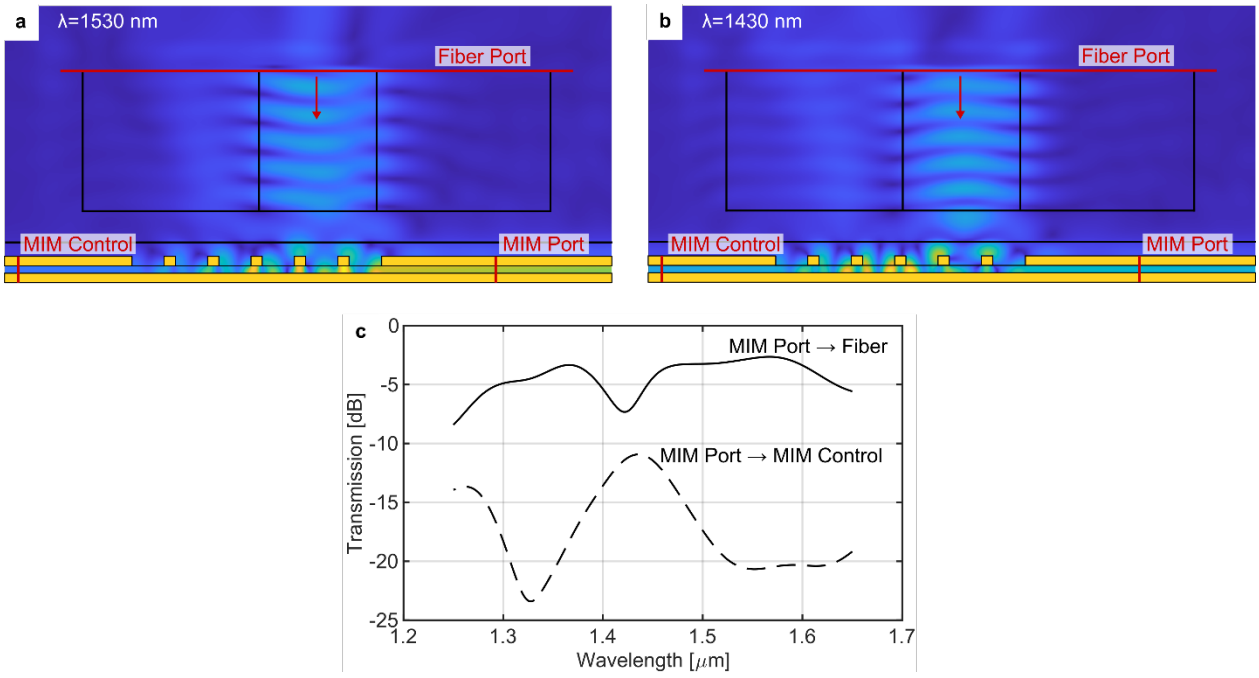


Figure S1: Modulus of the relevant out-of-plane *H*-field component. (a) The fiber port is excited at the transmission maximum at $\lambda = 1530$ nm. Most of the energy is transmitted to the right MIM waveguide. (b) At $\lambda = 1430$ nm, the energy is interacting more with the grating, less is transmitted to the right, and more to the left. (c) Transmission spectra from the right MIM waveguide to the fiber, and to the left MIM control waveguide, through the grating. The transmission maximum occurs at the coupling efficiency's minimum.

## 5. Study of Finite Grating Dimensions

The devices presented in this paper feature a waveguide width of 4 µm and grating bar widths of 8 µm. The grating consists of five bars, and the fiber has a mode field diameter of ~2 µm. It is interesting to investigate how the finite extension of the involved components influence the coupling efficiency, and how narrower and smaller gratings and waveguides would perform.

In a first simulation study, the number of grating bars has been swept from 0 to 5, and for each bar, the optimal lateral fiber position has been sought. In a second study, the fiber core diameter has been changed from 1.5 to 5 µm, and again a sweep of the fiber position has been carried out for each diameter. Figure S2 shows the results. It is interesting to note that a grating with only three grating bars has the highest coupling efficiency, with only little changes for more bars. In terms of mode field diameter, the smallest fiber core diameter of 1.5 µm yields the highest coupling efficiency, with only a slight decrease for larger diameters.

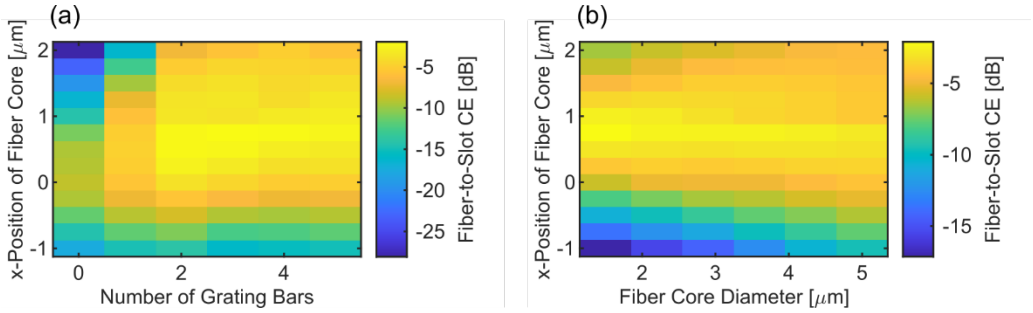


Figure S2: Maximum coupling efficiency of the grating (a) for a sweep of the number of grating bars and the lateral fiber position (negative shift: towards the MIM waveguide, positive shift: towards the grating), and (b) for a sweep of the fiber core diameter, influencing the mode field diameter of the incident fiber mode together with a sweep of the lateral fiber position.

Figure S3 shows the dependence of the maximum coupling efficiency on the width of waveguide and grating bars, as obtained by 3D simulations. A grating and waveguide width of both 2 µm yield the highest coupling efficiency, that plateaus at slightly lower levels for wider waveguide or wider grating. The results follow expectations, as the grating should be of the size of the fiber mode field diameter, which is 2 µm in our case.

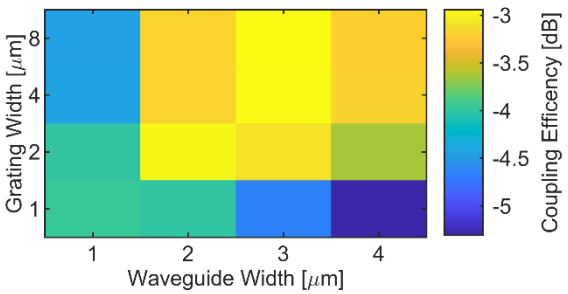


Figure S3: Maximum coupling efficiency of the grating for a sweep of waveguide and grating widths.

## 6. Optical Characterization

Two tunable laser sources (TLS) and optical power meters were used to determine the device insertion loss from 1270 to 1370 nm (covering the O-band), and from 1460 to 1640 nm (covering the S-, C-, and L-bands). Due to the fiber array's discrete core-to-core distance of 12 µm, only three device lengths (12, 24 and 36 µm) were available for optical cut-back measurements.

### Electro-Optical Characterization

The devices were optically probed as described above, while an electrical probe in ground-signal-ground configuration was used for the electrical probing. Figure S4 shows a schematic of the measurement. The devices were characterized in the O- and C-bands. An optical spectrum analyzer (OSA) was used to detect the optical sidebands induced by the applied radio-frequency (RF) signal. When the amplitude of the RF signal is known, the power ratio between optical sideband and carrier provides a direct measure of the phase modulator's $\pi$-voltage.[7]

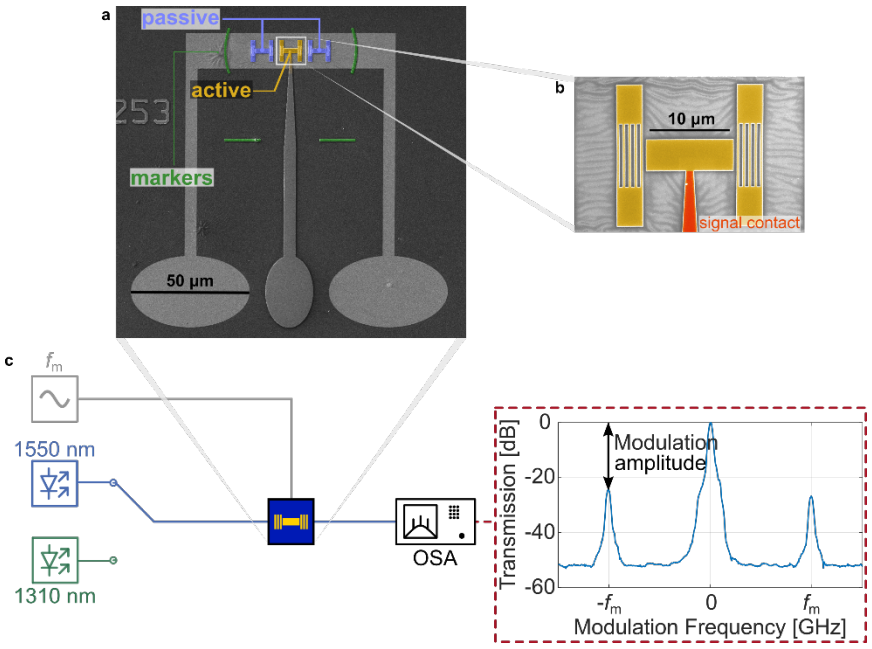


Figure S4: (a) SEM image of the active device, highlighted in yellow. Two passive devices are shown next to it, blue. (b). The narrow signal contact is highlighted in the zoom-in. (c) Schematic of the electro-optical characterization setup.

### Electro-Optical Bandwidth

The electro-optic bandwidth of the device has been measured in the setup shown in Figure S4, where the wavelength has been kept constant at a value of $\lambda = 1531$ nm and the frequency $f_m$ of the applied electrical signal has been swept. After calibrating for the losses in the RF branch (cable and GSG probe), the electro-optic frequency response of the device is found to be flat up to $f_m =$

70 GHz, see Figure S5. The 2-dB dip at 50 GHz stems probably from the electrode design. Future designs should incorporate a smaller spacing between signal and ground electrodes. RF simulations indicate an electro-optic 3-dB bandwidth of 400 GHz with an improved design of ground and signal electrodes.

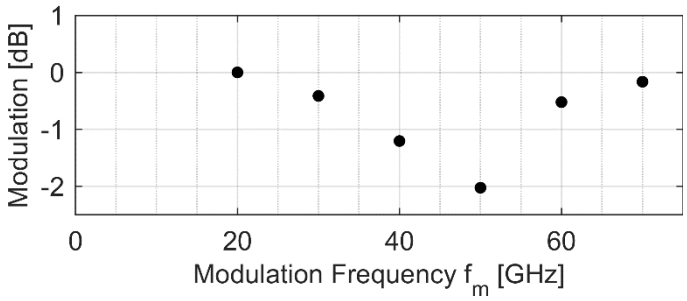


Figure S5: Electro-optic frequency response of the presented device. The electro-optic 3-dB bandwidth exceeds 70 GHz.

## 7. Data Measurements

The data modulation experiments were conducted in the C- and O-bands in a self-homodyne scheme. A random, $2^{17}$ bits long data sequence was loaded to the memory of a digital-to-analog converter with an analog bandwidth of 35 GHz (Micram DAC4[8]). The generated non-return-to-zero on-off keying (NRZ-OOK) electrical driving signal was electrically amplified. The applied peak-voltage at the modulator was 2.6 $V_p$.

Light from an external cavity laser (ECL), either at 1550 nm or at 1310 nm wavelengths, was coupled to the phase modulator was fed through a polarization controller and then coupled to the chip. The weaker output power of the ECL at 1310 nm has been compensated by a semiconductor optical amplifier (SOA), so that the incident optical power amounted to 7-10 dBm in both bands. The modulated light was amplified by fiber amplifiers (erbium-doped in the C-band and praseodymium-doped in the O-band), before it was guided to an optical coherent receiver and detected in a self-homodyne way. Balanced photodiodes with 70 GHz bandwidth were employed and fed two channels a real-time sampling oscilloscope with an electrical bandwidth of 63 GHz and a sampling rate of 160 GSa/s. All digital signal processing was performed offline. After timing and carrier recovery, an LMS equalizer with 101 filter taps was applied. The bit errors were counted and used to calculate the bit error ratio.

# 8. Bibliography


(1) Heni, W.; Haffner, C.; Cottier, R.; Fedoryshyn, Y.; Elder, D. L.; Dalton, L. R.; Leuthold, J. In *Dielectric Layers in Plasmonic-Organic Hybrid Modulators*, Advanced Photonics 2018 (BGPP, IPR, NP, NOMA, Sensors, Networks, SPPCom, SOF), Zurich, 2018/07/02; Optical Society of America: Zurich, 2018; p IW3B.3.

(2) Xu, H.; Liu, F.; Elder, D. L.; Johnson, L. E.; de Coene, Y.; Clays, K.; Robinson, B. H.; Dalton, L. R., Ultrahigh Electro-Optic Coefficients, High Index of Refraction, and Long-Term Stability from Diels–Alder Cross-Linkable Binary Molecular Glasses. *Chem Mater* **2020,** *32* (4), 1408-1421.

(3) Heni, W.; Kutuvantavida, Y.; Haffner, C.; Zwickel, H.; Kieninger, C.; Wolf, S.; Lauermann, M.; Fedoryshyn, Y. M.; Tillack, A.; Johnson, L. E.; Elder, D. L.; Robinson, B. H.; Freude, W.; Koos, C.; Leuthold, J.; Dalton, L. R., Silicon-Organic and Plasmonic-Organic Hybrid Photonics. *ACS Photonics* **2017,** *4* (7), 1576-1590.

(4) Lumerical Inc. https://www.lumerical.com/products/ (accessed Apr 19, 2021).

(5) Gao, L.; Lemarchand, F.; Lequime, M., Exploitation of multiple incidences spectrometric measurements for thin film reverse engineering. *Optics Express* **2012,** *20* (14), 15734-15751.

(6) Beadie, G.; Brindza, M.; Flynn, R. A.; Rosenberg, A.; Shirk, J. S., Refractive index measurements of poly(methyl methacrylate) (PMMA) from 0.4-1.6 µm. *Applied Optics* **2015,** *54* (31), F139-F143.

(7) Yongqiang, S.; Lianshan, Y.; Willner, A. E., High-speed electrooptic modulator characterization using optical spectrum analysis. *J. Light. Technol.* **2003,** *21* (10), 2358-2367.

(8) Schuh, K.; Buchali, F.; Idler, W.; Hu, Q.; Templ, W.; Bielik, A.; Altenhain, L.; Langenhagen, H.; Rupeter, J.; Duemler, U.; Ellermeyer, T.; Schmid, R.; Moeller, M. In *100 GSa/s BiCMOS DAC Supporting 400 Gb/s Dual Channel Transmission*, ECOC 2016; 42nd European Conference on Optical Communication, 18-22 Sept. 2016; 2016; pp 1-3.